

Solvation dynamics and electronic structure development of coumarin 120 in methanol: A theoretical modeling study

Koji Ando

Citation: *The Journal of Chemical Physics* **107**, 4585 (1997); doi: 10.1063/1.474801

View online: <http://dx.doi.org/10.1063/1.474801>

View Table of Contents: <http://scitation.aip.org/content/aip/journal/jcp/107/12?ver=pdfcov>

Published by the [AIP Publishing](#)

Articles you may be interested in

Born-Oppenheimer molecular dynamics and electronic properties of chlorophyll-c2 in liquid methanol
J. Chem. Phys. **138**, 225102 (2013); 10.1063/1.4808177

A first principles molecular dynamics study of lithium atom solvation in binary liquid mixture of water and ammonia: Structural, electronic, and dynamical properties
J. Chem. Phys. **134**, 024519 (2011); 10.1063/1.3511702

A polarizable mixed Hamiltonian model of electronic structure for micro-solvated excited states. I. Energy and gradients formulation and application to formaldehyde ($1A_2$)
J. Chem. Phys. **117**, 1242 (2002); 10.1063/1.1483858

Structures and electronic phases of the bis(ethylenedithio)tetrathiafulvalene (BEDT-TTF) clusters and κ -(BEDT-TTF) salts: A theoretical study based on ab initio molecular orbital methods
J. Chem. Phys. **111**, 5986 (1999); 10.1063/1.479894

Equilibrium structure, fluctuations, and spectroscopy of a solvated electron in methanol
J. Chem. Phys. **107**, 1970 (1997); 10.1063/1.474549



Solvation dynamics and electronic structure development of coumarin 120 in methanol: A theoretical modeling study

Koji Ando

*Institute of Materials Science, University of Tsukuba, Tsukuba, Ibaraki 305, Japan^{a)}
and The Institute of Physical and Chemical Research (RIKEN), Wako, Saitama 351-01, Japan*

(Received 31 March 1997; accepted 20 June 1997)

Electronic structure evolution of an organic dye coumarin 120 coupled to polar solvation dynamics is examined by combining *ab initio* electronic structure calculations and molecular dynamics (MD) simulations. Sets of nonorthogonal Hartree–Fock molecular orbitals optimized *in vacuo* and in dielectric continuum are utilized for a quantum mechanical description of the solute electronic polarization coupled to the solvent fluctuation. The adiabatic MD simulation for methanol solution is performed to evaluate the equilibrium and nonequilibrium dynamics of the (S_0 – S_1) energy gap coordinate and the dipole moments. The absorption and fluorescence spectra are computed via the spectral density functions obtained from the simulation analysis. The results for the quantum polarizable (Q-Pol) model of the solute probe are compared with those for a nonpolarizable fixed-charge (Fix-Z) model. It is shown that the solute electronic polarization notably affects the solvent-induced key quantities such as the reorganization energy, the spectral linewidth, and the Stokes shift (which are mutually related): For example, the computed Stokes shifts are ~ 2500 and ~ 4000 cm^{-1} for Fix-Z and Q-Pol, respectively. On the other hand, the solute polarization tends to slightly slow down the methanol solvation, which is not necessarily attributed to reduction of the “solvent force constant” because the effective mass of the coordinate is reduced as well. © 1997 American Institute of Physics. [S0021-9606(97)51136-6]

I. INTRODUCTION

Understanding the microscopic mechanisms of equilibrium and nonequilibrium solvation dynamics is a fundamental subject of chemical physics, being essential for determining rates and mechanisms of various chemical reactions and spectral line shapes of chromophores in solution. In particular, polar solute–solvent systems with strong and long-range electrostatic interaction have been studied most extensively.^{1–4} Among many theoretical and experimental studies, recent developments of the ultrafast laser spectroscopic techniques are advancing subpicosecond real-time information.³ Molecular dynamics (MD) simulations have also been performed to provide complementary information of model systems.^{4–11}

Early MD studies on solvation dynamics employed simple solute models such as spherical cavities and diatomics.^{5–7} Polyatomic models of solute were also developed, in which the electrostatic part of the solute–solvent interaction was represented by the Coulomb potential between effective point charges assigned to atomic sites.^{8–11} The charge parameters were usually determined from *ab initio* or semiempirical molecular orbital (MO) calculations of the isolated (gas-phase) solute molecules, and were often fixed constant in the solution phase simulations. Despite the neglect of seemingly critical aspects of real systems, the simulation results were demonstrated to agree quite well with experiments.¹⁰

There are at least two open questions, however, in the theoretical modeling aspect: (1) The solute probe molecules

change their electronic structure depending on the environmental polarization fluctuation. This effect can be particularly significant for electronic excited states. Then, what is the dynamical coupling between the solute electronic structure alteration and the polar solvation, and what are the consequences of this effect to be observed in experiments? (2) How do the intra- and intermolecular vibrational energy transfer processes affect the time-dependent spectra, and how do they couple and compete with the solvation process?

This paper explores primarily the first question by combining *ab initio* electronic structure calculations and MD simulations. A study on the second question is also under way and will be reported elsewhere. The first issue has been addressed recently by two groups, which employed diatomic and point-dipole solute models.^{12,13} We also note that the hybrid methods of semiempirical MO and MD calculations have good potential for elucidating these issues.¹⁴

In this work, we perform a theoretical molecular modeling of the solvation dynamics of coumarin 120 (C120) dye (Fig. 1) in methanol. An adiabatic simulation method, which makes use of sets of nonorthogonal *ab initio* MOs optimized isolated and in dielectric continuum, is developed to describe the electronic structure evolution of the solute coupled to the solvation dynamics. A straightforward way to account for the solute polarization effects would be to include the (classical) electrostatic interaction with the environment into the one-electron integrals of the Fock matrix of the solute and reoptimize the MOs (at every or some representative configuration).^{14,15} However, doing this at every MD step by the *ab initio* method is still computationally impractical for molecules as large as C120. Another way (though not very

^{a)}Present and permanent address.

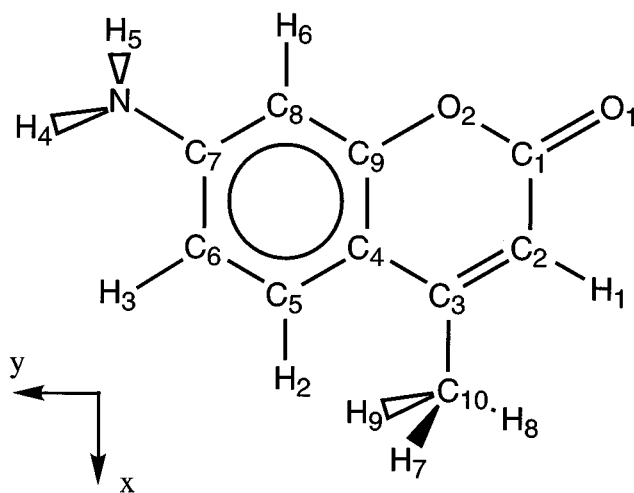


FIG. 1. The structure of coumarin 120 with the atom numbering used in Tables I, IV, and V.

straightforward) would be to construct diabatic electronic bases from the configuration interaction (CI) wave functions for several relevant states.¹⁶ On the other hand, the approximate method employed here would be a simple and efficient alternative.

7-amino coumarin dyes, which include efficient laser dyes emitting in the blue–green region,^{17,18} are often chosen as experimental probes for solvation dynamics studies^{10,19,20} because of their rather simple solvatochromic behavior^{21–23} with an isolated S_0 – S_1 excitation band and of their particularly large Stokes shift (~ 5000 cm^{–1}) in polar solvents. It is considered that the dipole moment is larger in the S_1 state than in the S_0 state since the $\pi\pi^*$ absorption maximum usually redshifts as the solvent polarity increases.²⁴ In terms of two valence-bond structures of a covalent and an ionic charge transfer (from the amino nitrogen to the carbonyl oxygen) forms, various characteristics of the 7-amino coumarins, such as the large dipole change upon photoexcitation

and the resulting marked Stokes shift, have been comprehended at least qualitatively.¹⁷

Among 7-amino coumarins, C153 and C102 (both with double alkane rings rigidizing the amino group) have been studied extensively by means of the ultrafast laser spectroscopies in a wide range of (nonpolar to polar) solvents.^{10,19,20} For aqueous solution, a study on C343[–] (with an ionic carboxyl group) has been reported.^{10(b)} Here we choose C120 for a model system, as it is the smallest 7-amino coumarin. We expect many of the conclusions obtained here would carry over and provide insights into the other related systems.

Section II summarizes the computational method. Section III discusses the simulation results. The static distribution functions of the energy gap coordinate and the dipole moments, as well as their mutual correlation, are investigated. The time-dependent evolutions of these quantities and the fluctuation–dissipation relation are then examined. The absorption and fluorescence spectra are computed by using the spectral density function derived from the simulation. Purely inhomogeneous spectral broadening²⁵ and the static Stokes shift are quantified for the present model. The time-dependent fluorescence spectra are also examined. Finally, comparison with a model with fixed atomic charges of the solute is described, which stresses the significance of the dynamical coupling between the solute electronic structures and the polar solvation. Section IV concludes the paper.

II. COMPUTATIONAL METHODS

The nuclear geometry of C120 in the S_0 state is first optimized by using the energy gradient method for the spin-restricted, closed-shell, Hartree–Fock (RHF) wave function with the semiempirical modified neglect of differential overlap (MNDO) approximation.²⁶ The atoms, except for the amino and methyl hydrogens, are constrained on a plane.²⁷ The resultant geometrical parameters are summarized in Table I, and are utilized throughout the present calculations.

TABLE I. Geometrical parameters of C120.

Bond distances ^a (Å)					
C ₁ –C ₂	1.480	C ₂ –C ₃	1.366	C ₃ –C ₄	1.473
C ₃ –C ₁₀	1.508	C ₄ –C ₅	1.420	C ₅ –C ₆	1.396
C ₆ –C ₇	1.425	C ₇ –C ₈	1.411	C ₇ –N	1.415
C ₈ –C ₉	1.421	C ₉ –O ₂	1.359	C ₁ –O ₂	1.382
C ₁ –O ₁	1.225				
Valence angles (deg.)					
C ₂ C ₁ O ₁	128.0	C ₂ C ₃ C ₁₀	120.7	C ₆ C ₇ N	120.1
C ₁ C ₂ H ₁	115.3	C ₄ C ₅ H ₂	120.4	C ₅ C ₆ H ₃	118.8
C ₇ C ₈ H ₆	121.0	C ₇ NH _{4,5}	112.8, 113.0		
C ₃ C ₁₀ H _{7–9}	111.0, 111.0, 112.1				
Torsional angles (deg.)					
C ₆ C ₇ NH _{4,5}		–31.2, –153.7			
C ₂ C ₃ C ₁₀ H _{7–9}		119.8, 0.2, –119.5			

^aCH bond lengths at the rings are all 1.091 Å. CH bond lengths in the –CH₃ group are 1.110, 1.109, and 1.110 Å for H_{7–9}. NH bond lengths in the –NH₂ group are both 1.006 Å.

TABLE II. Total energies and dipole moments of isolated C120 from RHF, ROHF, and S-CI calculations.

	ϕ_{np}^0	ϕ_{np}^1	S-CI ^a
Energy ^b	-587.1868	-587.0659	-586.9972
Dipole moment ^c			
μ_x	4.81	4.13	3.63
μ_y	5.33	3.85	7.16
μ_z	1.60	1.59	1.56

^aFor the S_1 state with ϕ_{np}^0 orbitals.^bIn hartree. The nuclear repulsion energy is 739.9051 hartree.^cIn debye. The C₉-C₄ bond is on the x axis (Fig. 1).

In the adiabatic simulation, the electronic wave functions of the solute C120 as a function of the (time-dependent) solute-solvent configuration $\mathbf{S}(t)$ are described by a superposition of “nonpolarized” and “polarized” electronic bases ($|\phi_{np}\rangle$ and $|\phi_{pol}\rangle$) for S_0 and S_1 states (that are specified below). Namely, the solute electronic polarization induced by the configuration \mathbf{S} is described dynamically in terms of the variation of the mixing coefficients of these diabatic bases. To do this, as outlined below, the electronic Hamiltonian matrix on the $|\phi_{np}\rangle$ and $|\phi_{pol}\rangle$ diabatic bases is constructed to be diagonalized at each configuration of the simulation step. The interaction potentials and forces are updated according to the mixing coefficients.

There could be several choices for the diabatic electronic bases. Diabatization of CI wave functions of relevant adiabatic states would be useful for systems of moderate size.¹⁶ Alternatively, we employ *ab initio* RHF (for S_0) and open-shell ROHF (for S_1) MO Slater determinants optimized *in vacuo* and in dielectric continuum.^{28,29} The polarized functions are computed by the self-consistent reaction-field (SCRf) method.³⁰ Since the four functions (which we denote $|\phi_{np}^0\rangle$, $|\phi_{np}^1\rangle$, $|\phi_{pol}^0\rangle$, and $|\phi_{pol}^1\rangle$) are optimized independently, they are not orthogonal to each other. Thus we compute the Hamiltonian (and dipole) matrix elements among them via the method of corresponding orbital transformation.³¹

The use of the nonorthogonal Slater determinants might appear rather unusual. Indeed, it has been demonstrated to provide efficient ways to compactly describe the electron correlation effects.³² As shown in Appendix A, the polarized function $|\phi_{pol}\rangle$ essentially includes (or overlaps with) the excitation configurations built from the MOs of nonpolarized $|\phi_{np}\rangle$. Therefore, for example, the *in vacuo* wave function is variationally improved by mixing these bases, as in the non-orthogonal CI³² methods.

The MIDI4 atomic orbital (AO) basis set³³ of the split-valence quality is employed. The number of the AO basis function is 135 for C120. The S_1 wave function $|\phi_{np}^1\rangle$ is assumed to be described by a $\pi\pi^*$ -type configuration, which is verified from a preliminary single-excitation CI (S-CI) calculation.³⁴ In the SCRf calculations, the static dielectric constant³⁵ of 78.4 and the spherical cavity of 3.5 Å radius³⁶ are utilized. The resultant energies and dipole moments for

TABLE III. Energies and dipole moments of the polarized electronic wave functions of C120 from SCRf(RHF/ROHF) calculations.

	ϕ_{pol}^0	ϕ_{pol}^1
Total energy ^a	-587.2161	-587.0817
Reaction-field energy ^a	-0.0622	-0.0284
Dipole moment ^b		
μ_x	8.03	6.43
μ_y	12.98	7.95
μ_z	1.94	1.92

^aIn hartree. The nuclear repulsion energy is 739.9051 hartree.^bIn debye. The C₉-C₄ bond is on the x axis (Fig. 1).

the diabatic bases $|\phi_{np}\rangle$ and $|\phi_{pol}\rangle$ are summarized in Tables II and III.³⁷

The electronic Hamiltonian matrix for the solute is expressed by

$$\mathbf{H}(\mathbf{S}) = \mathbf{H}^0 + \tilde{\mathbf{V}}(\mathbf{S}), \quad (2.1)$$

where \mathbf{H}^0 denotes the solute intramolecular part that is independent of \mathbf{S} and should be computed only once prior to the adiabatic simulations.³⁸ The solute-solvent interaction matrix $\tilde{\mathbf{V}}(\mathbf{S})$ is modeled by

$$\begin{aligned} [\tilde{\mathbf{V}}(\mathbf{S})]_{IJ} &= \langle I | \tilde{\mathbf{V}}(\mathbf{S}) | J \rangle \\ &= \sum_{a,i} \left[\frac{Z_a^{IJ} Z_i}{r_{ai}} + 4 \epsilon_{ai} \left\{ \left(\frac{\sigma_{ai}}{r_{ai}} \right)^{12} - \left(\frac{\sigma_{ai}}{r_{ai}} \right)^6 \right\} \langle I | J \rangle \right] \\ (I, J) &= \phi_{np}^{0,1}, \phi_{pol}^{0,1}, \end{aligned} \quad (2.2)$$

where the subscripts a and i denote the atom sites of the solute and solvent molecules, respectively, and r_{ai} is the distance between them. The diagonal elements Z_a^{II} are the effective point charges on the atoms of C120 for the diabatic basis I , which are determined by the least-squares fitting to reproduce the electrostatic potentials (ESPs) around the molecule generated from the electronic wave functions.^{39(a)} The ESPs are computed at 1009 points on four layers of the Connolly surface^{39(b)} at 1.5, 3.0, 4.5, and 6.0 times the van der Waals radii of the constituent atoms.

The off-diagonal charges Z_a^{IJ} are also determined by fitting to reproduce the off-diagonal “exchange field” potential⁴⁰

$$\begin{aligned} V_{\text{ex}}(\mathbf{R}) &= \langle I | \sum_k \frac{1}{|\mathbf{R} - \mathbf{r}_k|} | J \rangle + V_{\text{ex}}^{\text{nuc}}(\mathbf{R}) \\ &= C \sum_{\mu\nu} \mathbf{P}_{\mu\nu} \langle \mu | \frac{1}{|\mathbf{R} - \mathbf{r}|} | \nu \rangle + V_{\text{ex}}^{\text{nuc}}(\mathbf{R}). \end{aligned} \quad (2.3)$$

In the second equation, μ and ν denote the AOs, \mathbf{r} is the electron position operator, and \mathbf{P} is the generalized MO density matrix^{31(b)} obtained via the corresponding orbital transformation of the nonorthogonal Slater determinants. C

TABLE IV. Charge parameters for the Q-Pol and Fix-Z models (round off to three decimals). Only the diagonal elements Z_a'' are listed for Q-Pol. The charges for Fix-Z are obtained from the equilibrium average of the Q-Pol simulations.

Atom	Q-Pol				Fix-Z	
	ϕ_{np}^0	ϕ_{np}^1	ϕ_{pol}^0	ϕ_{pol}^1	S_0	S_1
C ₁	1.325	1.399	1.095	1.130	1.315	1.014
C ₂	-0.995	-1.149	-0.524	-0.477	-0.826	-1.035
C ₃	0.643	0.726	0.471	0.370	0.523	0.934
C ₄	-0.591	-0.630	-0.581	-0.545	-0.576	-0.675
C ₅	0.213	0.208	0.168	0.188	0.208	0.158
C ₆	-0.682	-0.566	-0.647	-0.602	-0.654	-0.536
C ₇	0.709	0.740	0.706	0.737	0.711	0.773
C ₈	-0.675	-0.701	-0.619	-0.621	-0.664	-0.649
C ₉	0.695	0.678	0.655	0.582	0.633	0.831
C ₁₀	-0.385	-0.345	-0.377	-0.341	-0.360	-0.402
N	-0.980	-0.974	-0.985	-1.018	-0.989	-0.978
O ₁	-0.729	-0.904	-0.659	-0.775	-0.768	-0.756
O ₂	-0.675	-0.701	-0.619	-0.621	-0.664	-0.649
H ₁	0.291	0.253	0.191	0.163	0.249	0.208
H ₂	0.119	0.159	0.132	0.161	0.136	0.150
H ₃	0.257	0.303	0.248	0.285	0.275	0.251
H ₄	0.394	0.452	0.390	0.440	0.416	0.410
H ₅	0.393	0.401	0.396	0.404	0.396	0.404
H ₆	0.266	0.232	0.262	0.230	0.252	0.251
H ₇	0.119	0.130	0.100	0.100	0.116	0.110
H ₈	0.136	0.096	0.124	0.098	0.116	0.127
H ₉	0.098	0.154	0.080	0.124	0.112	0.114

$= \pm 1$ is a phase factor from the orbital transformation matrices.^{31(b)} The term $V_{ex}^{nuc}(\mathbf{R})$ represents the Coulomb potential from the bare nuclei of the solute factored by the overlap $\langle I|J \rangle$.

The short-range exchange-exclusion term, which is modeled by the 12-6 Lennard-Jones (LJ) from in Eq. (2.2), is assumed to be common among the diabatic bases. Note that the overlap factor $\langle I|J \rangle$ is present for the LJ term, which is, on the other hand, implicitly included in the exchange field of Eq. (2.3). The LJ parameters ϵ and σ are taken from the optimized potentials for liquid simulations (OPLS) model⁴¹ of the protein amino acids. The OPLS model is also utilized for the solvent methanol;^{41(c)} $Z_{Me}=0.265e$, $Z_O=-0.700e$, $Z_H=0.435e$, $\epsilon_{MeMe}=0.207$, $\epsilon_{OO}=0.170$, $\sigma_{MeMe}=3.775$, $\sigma_{OO}=3.070$, where ϵ and σ are given in kilocalories per mole and angstroms, respectively. The standard combining rule such as $\epsilon_{ab}=\sqrt{\epsilon_{aa}\epsilon_{bb}}$ is employed for both the ϵ and σ parameters. The charge and the LJ parameters, the latter with the assumed correspondence to the amino acid's atom types, are listed in Tables IV and V.⁴²

The solute C120 is immersed in 350 solvent methanol molecules. The truncated octahedron periodic boundary condition^{43(a),43(b)} is employed, which nearly approximates the isotropic environment of the unimolecular reaction and extends for a larger distance between the periodic images than the cubic box at a given number density. The total mass density is set to be 0.759 g/cm³, which is taken from a constant pressure Monte Carlo simulation^{41(c)} for liquid OPLS methanol (at the standard condition). The distance between the periodic images is then 36.8 Å.

Both C120 and methanol are treated as rigid bodies in

the simulation. Quaternion parameters are utilized to describe the rotational motion of the molecules.^{43(a)} The classical equations of motion of the nuclei are numerically integrated by the Gear predictor-corrector method^{43(c)} which is initiated by the fourth-order Runge-Kutta method.^{43(d)} The five- and four-values Gear algorithms are employed for the rotational and translational equations of motion, respectively. As outlined above, the electronic part of the solute is solved at every simulation step⁴⁴ and the charge parameters are determined from the mixing coefficient of the diabatic bases that update the interaction potentials and forces. The pair

TABLE V. Lennard-Jones potential parameters for C120 and their correspondence to OPLS atom types of amino acids. ϵ and σ are given in kcal/mol and in Å, respectively.

Atom ^a	C120		Amino acids		
	ϵ	σ	Atom/group R	Residue	Type ^b
C ₁	0.105	3.750	C ^{γ}	Asp	17
C _{2,5,6,8}	0.110	3.750	CH ^{δ,ϵ,ζ}	Phe	11
C ₃	0.110	3.750	C ^{γ}	Phe	11
C ₄	0.145	3.750	C ^{δ}	Trp	50
C ₇	0.145	3.750	C ^{ϵ}	Trp	45
C ₉	0.110	3.750	C ^{ζ}	Tyr	26
C ₁₀	0.160	3.910	CH ₃ ^{β}	Ala	7
N	0.170	3.250	N ^{δ}	Asn	12
O ₁	0.210	2.960	O ^{δ}	Asp	18
O ₂	0.195	3.047	ROR ^{γ}

^aCH (ring), -NH₂ and -CH₃ parts are treated as extended atoms.

^bReference 41(a).

^cReference 41(b).

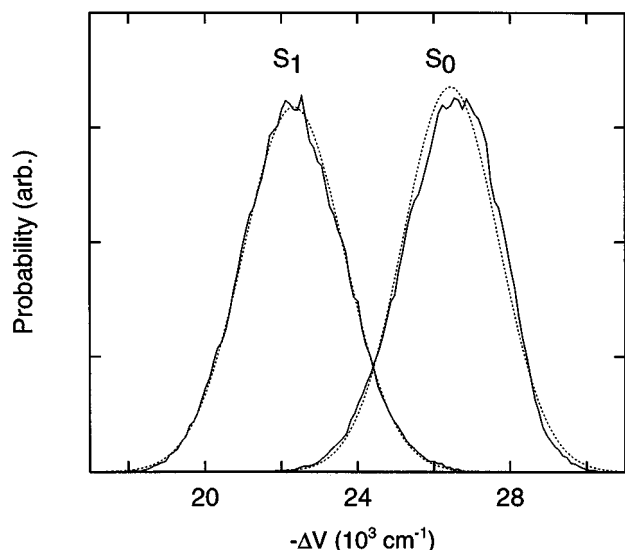


FIG. 2. Probability distribution functions $P_I(\Delta V)$ of the energy gap coordinate ΔV in S_I state ($I = 0, 1$). Dotted curves are the Gaussian approximation of Eq. (3.4).

interaction potentials are smoothly truncated⁹ in the region $0.9 r_{\text{cut}} < r_{\text{cm}} < r_{\text{cut}}$ where r_{cm} is the distance between the centers of mass of two interacting molecules. The cutoff distance r_{cut} is taken to be $\sqrt{3}/4$ of the distance between the periodic images.

Equilibrium MD calculations are carried out for 450 ps for each of the S_0 and S_1 states with a time step $\Delta t = 0.5$ fs, after a series of cooling and equilibration runs.⁴⁵ In the course of the equilibrium MD run for the S_0 state, the configurations and velocities of the system are sampled and are to be used for the initial conditions of the nonequilibrium trajectory calculations on the S_1 surface. Two-hundred configurations are sampled with random^{43(d)} intervals of at least 1 ps. No temperature controlling is employed for both the equilibrium and nonequilibrium simulations. The kinetic temperature of the (microcanonical) system in the equilibrium simulation was 301 and 300 K for the S_0 and S_1 states, respectively, with the rms fluctuation of ~ 7 K. The rms deviations of the total energy were 0.9 (S_0) and 2.5 (S_1) kcal/mol.

III. RESULTS AND DISCUSSION

A. Static properties

Figure 2 shows the equilibrium distribution functions $P_I(\Delta V)$ of the energy gap coordinate

$$\Delta V = H_0 - H_1 = V_0 - V_1, \quad (3.1)$$

where H_I and V_I denote the (electronically adiabatic) Hamiltonian and potential energy for the nuclear coordinates in the S_I state. Here and hereafter, the subscript I denotes the state label ($I = 0, 1$). We consider two kinds of reorganization energy.⁴⁶ One is given by

$$\lambda = (-\langle \Delta V \rangle_0 + \langle \Delta V \rangle_1)/2, \quad (3.2)$$

TABLE VI. Reorganization energies, free energy gap, and characteristic frequencies computed from equilibrium simulations of Q-Pol and Fix-Z models.

	Q-Pol	Fix-Z
λ (kcal/mol)	5.88 ± 0.38	3.71 ± 0.22
λ_0 (kcal/mol)	10.66	4.08
λ_1 (kcal/mol)	11.88	4.21
ΔF_0 (10^3 cm^{-1})	24.38 ± 0.13	26.28 ± 0.08
Ω_0 (cm^{-1})	154 ± 11	174 ± 10
Ω_1 (cm^{-1})	172 ± 12	183 ± 13

in which $\langle \cdots \rangle_I$ denotes the equilibrium average in the S_I state. Equation (3.2) represents the (free) energy increase of the S_0 state when the system is brought from the equilibrium configuration of the S_0 state to that of the S_1 state. The other definition is given in terms of the (classical) thermal fluctuation of ΔV ,

$$\lambda'_I = \langle \delta \Delta V^2 \rangle_I / 2k_B T, \quad (3.3)$$

where $k_B T$ denotes the Boltzmann temperature and $\delta \Delta V \equiv \Delta V - \langle \Delta V \rangle_I$. This corresponds to the width of $P_I(\Delta V)$ and to (half) the inverse of the “force constant” of the free energy curves in the ΔV coordinate [see Eqs. (3.6) and (3.16)]. λ and λ'_I coincide for exactly parabolic free energy curves. The computed values are listed in Table VI.

The dotted curves in Fig. 2 are the Gaussian approximation,

$$\bar{P}_I(\Delta V) \propto \exp \left[-\frac{(\Delta V - \langle \Delta V \rangle_I)^2}{4k_B T \lambda'_I} \right]. \quad (3.4)$$

The simulated results of $P_I(\Delta V)$ show slightly asymmetric deviation from the Gaussians. These small deviations in the S_0 and S_1 states appear to incline toward outer regions of each distribution.⁴⁷ (This is also seen in the nonequilibrium time-dependent distribution functions examined in Sec. III D.) This behavior would be connected to the relation

$$F_0(\Delta V) - F_1(\Delta V) = \Delta V, \quad (3.5)$$

where $F_I(\Delta V)$ denotes the free energy function given by

$$F_I(\Delta V) = -k_B T \ln P_I(\Delta V) + \text{const.} \quad (3.6)$$

Note that Eq. (3.5) is precise regardless of whether the distribution is Gaussian or not.⁴⁸ We also point out below that Eq. (3.5) is closely related to the Einstein relation of the absorption and fluorescence spectra [see Eq. (3.15)].

Figure 3 shows the correlation between ΔV and the absolute dipole moments $|\mathbf{d}_0|$, $|\mathbf{d}_1|$ and the transition dipole $|\mathbf{d}_t|$. The dipole moments correlate to ΔV almost linearly though weakly. The equilibrium averages and the variances of the dipole moments are summarized in Table VII.

B. Solvation dynamics

Figure 4 displays the (classical) equilibrium time correlation functions (TCFs):

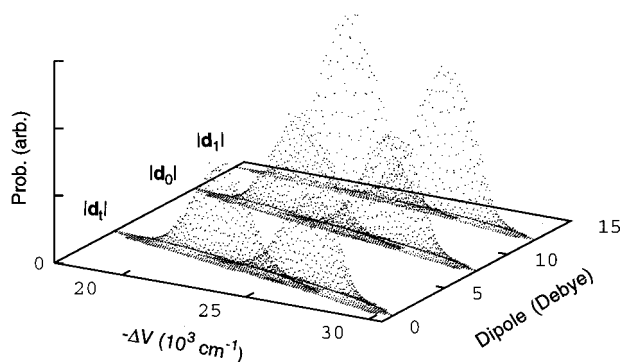


FIG. 3. A three-dimensional plot of the probability distribution as a function of the energy gap ΔV and the (absolute) dipole moments \mathbf{d}_0 , \mathbf{d}_1 and the transition dipole \mathbf{d}_t . Peaks in the smaller $-\Delta V$ region are from the equilibrium simulation in S_1 state, as in Fig. 2.

$$\Phi_I(t) = \frac{\langle \delta \Delta V(0) \delta \Delta V(t) \rangle_I}{\langle \delta \Delta V(0)^2 \rangle_I} \quad (I=0,1), \quad (3.7)$$

and the nonequilibrium response function:

$$\Psi_{01}(t) = \frac{\langle \Delta V(t) \rangle_{01} - \langle \Delta V(\infty) \rangle_{01}}{\langle \Delta V(0) \rangle_{01} - \langle \Delta V(\infty) \rangle_{01}}, \quad (3.8)$$

in which $\langle \Delta V(t) \rangle_{01}$ denotes the ensemble average of the nonequilibrium trajectories at time t after $S_1 \leftarrow S_0$ excitation. We put $\langle \Delta V(\infty) \rangle_{01} \equiv \langle \Delta V \rangle_1$. As seen in Fig. 4, $\Phi_0(t)$, $\Phi_1(t)$, and $\Psi_{01}(t)$ agree well within the simulation uncertainties, indicating the linear response of the system.

Many of the previous simulation studies of methanol solvation dynamics demonstrated marked nonlinear behavior compared to the present results. The less significant nonlinearity of the present system is not surprising considering the rather small dipole change upon photoexcitation, and consequently less energetic perturbation.^{49,50}

Figure 4 also includes the TCF of the transition dipole \mathbf{d}_t projected onto and averaged over the space-fixed frame, $\tilde{d}_t \equiv \frac{1}{3} \sum_{i=1}^3 \mathbf{d}_t \cdot \mathbf{e}_i$, where \mathbf{e}_{1-3} denote unit vectors in the three

TABLE VII. Equilibrium averages and variances of the body-fixed Cartesian components and the absolute values of the dipole moments (in debye) in the S_0 and S_1 states. The C₉–C₄ bond is on the x axis (Fig. 1).

	X	$\langle X \rangle_0$	$\sqrt{\langle \delta X^2 \rangle_0}$	$\langle X \rangle_1$	$\sqrt{\langle \delta X^2 \rangle_1}$
\mathbf{d}_0	d_{0x}	5.48	0.15	5.91	0.15
	d_{0y}	6.52	0.35	7.53	0.35
	d_{0z}	1.73	0.02	1.78	0.02
	$ \mathbf{d}_0 $	8.69	0.36	9.74	0.36
\mathbf{d}_1	d_{1x}	6.96	0.09	7.20	0.07
	d_{1y}	10.96	0.24	11.58	0.19
	d_{1z}	1.74	0.01	1.76	0.01
	$ \mathbf{d}_1 $	13.10	0.26	13.75	0.19
\mathbf{d}_t	d_{tx}	0.70	0.16	1.15	0.15
	d_{ty}	2.15	0.38	3.22	0.35
	d_{tz}	-0.02	0.02	0.02	0.02
	$ \mathbf{d}_t $	2.27	0.41	3.42	0.38

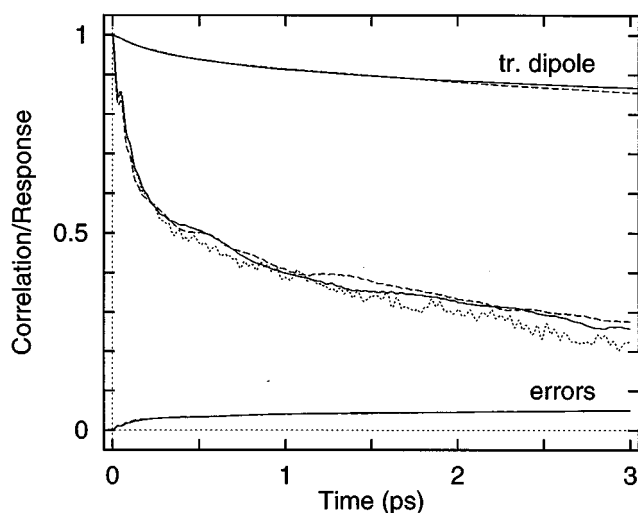


FIG. 4. The time correlation and the response functions $\Phi_0(t)$ (solid line), $\Phi_1(t)$ (dashed line) and $\Psi_{01}(t)$ (dotted line). Estimated simulation uncertainties [cf. Chap. 6 of Ref. 43(a)] and the time correlation of the transition dipole \tilde{d}_t are also included, for which the line types correspond to those for $\Phi_I(t)$.

Cartesian directions. This decays slowly compared to the characteristic time scale of ΔV . In fact, the TCF of the absolute $|\mathbf{d}_t|$ is seen to correlate well with that of ΔV . However, the time decay of the space-projected \tilde{d}_t is slow because it is controlled by the rotational motion of the body-fixed frame of the probe molecule. We thus employ the Condon approximation to compute the first-order optical spectra in Sec. III C.

The ensemble average of the nonequilibrium evolutions of the dipoles $\langle |\mathbf{d}_1(t)| \rangle_{01}$, $\langle |\mathbf{d}_t(t)| \rangle_{01}$, and $\langle \tilde{d}_t(t) \rangle_{01}$, are displayed in Fig. 5. The developments of $|\mathbf{d}_1|$ and $|\mathbf{d}_t|$ are seen

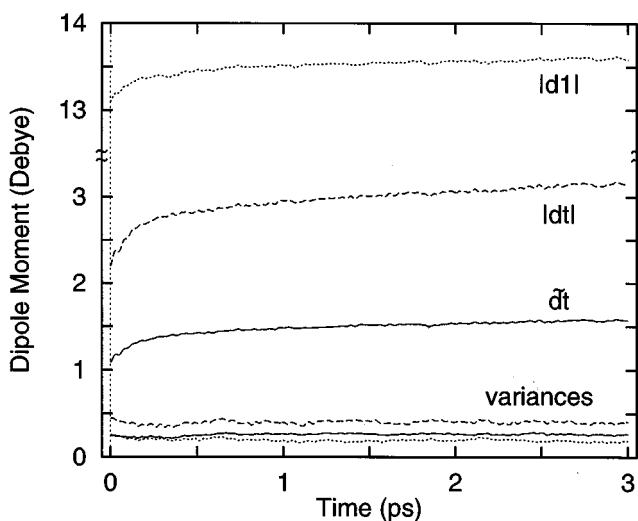


FIG. 5. Ensemble averages of the nonequilibrium development after the $S_1 \leftarrow S_0$ excitation of $|\mathbf{d}_1|$ (dotted line), $|\mathbf{d}_t|$ (dashed line), and \tilde{d}_t (solid line). The variances of the ensemble averages are also displayed with the corresponding line types.

to correlate well with $\Psi_{01}(t)$ in Fig. 4, while both the value and the increase of \bar{d}_t are notably smaller.

C. Absorption and fluorescence spectra

The absorption and fluorescence spectra are described in terms of the TCF formalism of the golden-rule perturbation theory⁵¹ by

$$I_{\text{ab}}(\omega) = \frac{|M_{\text{ab}}|^2}{\hbar^2} \int_{-\infty}^{+\infty} dt \exp \left[-i(\omega + \langle \Delta V \rangle_0 / \hbar) t \right. \\ \left. + \left(\frac{i}{\hbar} \right)^2 \int_0^t d\tau_1 \int_0^{\tau_1} d\tau_2 \langle \delta \Delta V(\tau_2) \delta \Delta V(\tau_1) \rangle_0 \right], \quad (3.9)$$

$$I_{\text{fl}}(\omega) = \frac{|M_{\text{fl}}|^2}{\hbar^2} \int_{-\infty}^{+\infty} dt \exp \left[+i(\omega + \langle \Delta V \rangle_1 / \hbar) t \right. \\ \left. + \left(\frac{i}{\hbar} \right)^2 \int_0^{-t} d\tau_1 \int_0^{\tau_1} d\tau_2 \langle \delta \Delta V(\tau_1) \delta \Delta V(\tau_2) \rangle_1 \right], \quad (3.10)$$

in which M_{ab} and M_{fl} are the appropriate transition dipole moments.⁵² Here the TCFs are quantum mechanical and $\Delta V(t) \equiv e^{iH_I t / \hbar} \Delta V e^{-iH_I t / \hbar}$ in $\langle \cdots \rangle_I$.

The quantum TCFs in Eqs. (3.9) and (3.10) are evaluated from the MD trajectory data as follows: First, we define the Fourier transforms of the quantum and classical TCFs, $G^q(\omega)$ and $G^{\text{cl}}(\omega)$,

$$\langle \delta \Delta V(0) \delta \Delta V(t) \rangle_I^\alpha = \frac{1}{2\pi} \int_{-\infty}^{\infty} d\omega e^{-i\omega t} G_I^\alpha(\omega), \quad (3.11)$$

where the superscripts $\alpha = q$ or cl denote the quantum and classical TCFs, respectively. Here, we assume the following quantum-classical correspondence between $G^q(\omega)$ and $G^{\text{cl}}(\omega)$,

$$G^q(\omega) = \frac{\beta \hbar \omega}{e^{\beta \hbar \omega} - 1} G^{\text{cl}}(\omega) \quad (\beta \equiv 1/k_B T), \quad (3.12)$$

which is exact for harmonic systems and is expected to be reasonable for weakly anharmonic bound potentials. The spectra are then given in terms of the quantities available from the MD data by

$$I_{\text{ab}}(\omega) = \frac{|M_{\text{ab}}|^2}{\hbar^2} \int_{-\infty}^{+\infty} dt \exp \left[-i(\omega - \Delta F^0 / \hbar) t \right. \\ \left. + \frac{i}{\hbar} (\lambda - \lambda'_0) t + \frac{\beta}{2\pi \hbar} \int_0^\infty d\omega \frac{G_0^{\text{cl}}(\omega)}{\omega} \right. \\ \left. \times \left\{ (\cos \omega t - 1) \coth \left(\frac{\beta \hbar \omega}{2} \right) + i \sin \omega t \right\} \right], \quad (3.13)$$

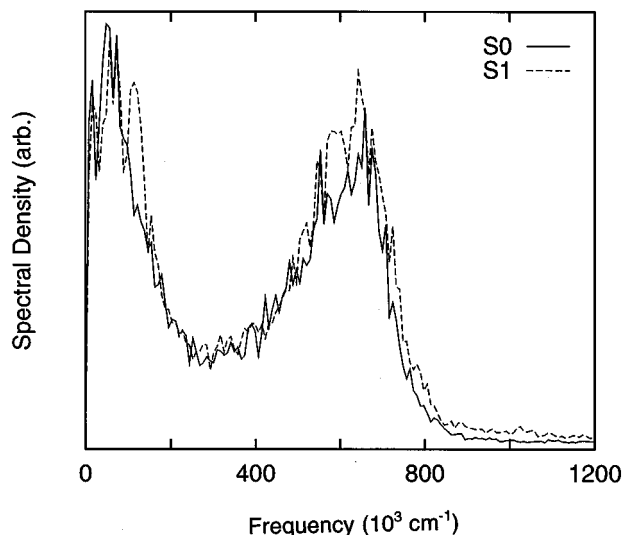


FIG. 6. Spectral density function $J(\omega)$ normalized by the integral $\int_0^\infty [J(\omega)/\omega] d\omega$ which relates to the reorganization energy λ via Eq. (A4). The solid and dashed lines are for S_0 and S_1 states, respectively. See Appendix B for the relation to $G^q(\omega)$ and $G^{\text{cl}}(\omega)$.

$$I_{\text{fl}}(\omega) = \frac{|M_{\text{fl}}|^2}{\hbar^2} \int_{-\infty}^{+\infty} dt \exp \left[+i(\omega - \Delta F^0 / \hbar) t \right. \\ \left. + \frac{i}{\hbar} (\lambda - \lambda'_1) t + \frac{\beta}{2\pi \hbar} \int_0^\infty d\omega \frac{G_1^{\text{cl}}(\omega)}{\omega} \right. \\ \left. \times \left\{ (\cos \omega t - 1) \coth \left(\frac{\beta \hbar \omega}{2} \right) + i \sin \omega t \right\} \right], \quad (3.14)$$

in which $\Delta F^0 \equiv (-\langle \Delta V \rangle_0 - \langle \Delta V \rangle_1) / 2$ corresponds to the free energy gap between the S_0 and S_1 equilibrium states. For exactly harmonic systems, the term $\lambda - \lambda'_I$ vanishes. The time integrals of the oscillatory functions in Eqs. (3.13) and (3.14) are evaluated by using the method of steepest descents, which is almost isomorphic with the computation of nonadiabatic electron transfer rates.⁵³ The imaginary time saddle point is evaluated numerically by the Newton–Raphson method.^{43(d)}

Figure 6 displays the spectral density function $J(\omega)$ computed from the cosine transform of the classical MD trajectory.⁵⁴ [We present $J(\omega)$ rather than $G(\omega)$ just because of the former's prevalence in the literature: See Appendix B.] The broadband peaked around 700 cm^{-1} comes from the libration of the methanol hydroxyl part that contributes to the initial fast decay and subsequent weak oscillation^{6,9,55} of the TCF in Fig. 4.

The computed absorption and fluorescence spectra are displayed in Fig. 7. The dotted curves are the Gaussians of the classical limit $\beta \hbar \rightarrow 0$. In terms of the “photon-dressed state” perspective, the deviation of the spectra from the Gaussians can be ascribed to the nuclear tunneling effect from the photon-dressed state. This is in analogy with the

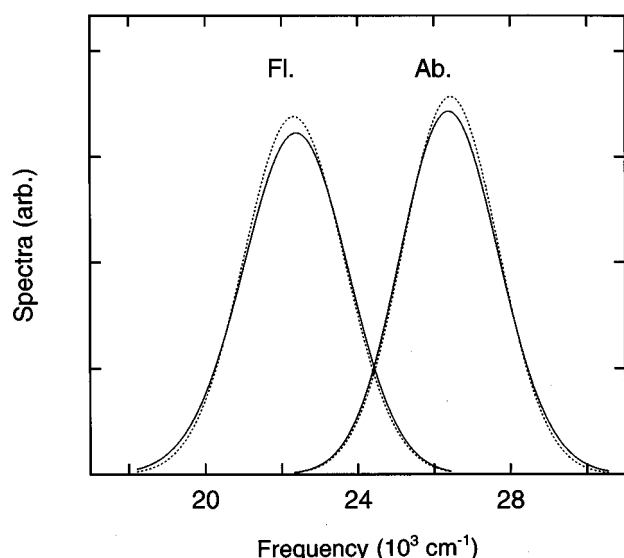


FIG. 7. Computed absorption and fluorescence spectra that represent purely solvent-induced linewidth and Stokes shift (i.e., without vibronic structures). The dotted curves are the corresponding classical ($\beta\hbar \rightarrow 0$) Gaussian limits.

deviation of the electron transfer rates' energy gap law from inverted parabola due to nuclear tunneling effects.⁵³

The full width at half-maximum (FWHM) and the peaks distance (Stokes shift) of the spectra are listed in Table VIII. Close resemblance between the spectral line shapes and the distribution functions $P_I(\Delta V)$ in Fig. 2 is noted. This implies that the system is in the so-called "static" or "strong-coupling" limit.⁵⁶ This is also rationalized straightforwardly from the other (classical) results herein, indicating $\tau_c \sqrt{\langle \delta \Delta V^2 \rangle} / \hbar \gg 1$, where τ_c denotes the correlation time of the TCFs in Fig. 4. [See also Eq. (3.3) and Table IV.] It would also be intriguing to note that the Einstein relation,⁵⁶

$$I_{ab}(\omega) \propto I_{fl}(\omega) \exp(\hbar \omega / k_B T), \quad (3.15)$$

is immediately derived from the free energy relation Eq. (3.5) in the static limit.

Since the solute C120 is treated as a rigid body in the present calculation, the spectral widths in Fig. 7 represent (or extract) only the "inhomogeneous,"²⁵ broadening coming from the solvent thermal fluctuation. The other homogeneous mechanisms such as the natural and collision-induced lifetimes of the excited state might further affect the line shape,

TABLE VIII. Peak positions ν_{\max} , FWHM, and Stokes shift of the computed absorption and fluorescence spectra (in 10^3 cm^{-1}) for the Q-Pol and Fix-Z models.

		Q-Pol	Fix-Z
Absorption	ν_{\max}	26.4	27.5
	FWHM	3.0	1.9
Fluorescence	ν_{\max}	22.4	25.1
	FWHM	3.2	1.9
Stokes shift		4.0	2.5

which could be taken into account by, e.g., inserting an exponential decay factor into Eqs. (3.13) and (3.14) in some phenomenological way. A possible improvement of the model by developing flexible models of both the solute and solvent species is briefly discussed in Sec. IV.

D. Time-dependent spectra

Section III C demonstrated that the static first-order spectra of the present system are well described by the "strong-coupling" case. This implies that the time scales for the photon absorption/emission are much shorter than those for the relevant nuclear motions. We postulate here that this also applies for the (nonequilibrium) time-dependent fluorescence (TDF) spectra, which would be reasonable considering the nearly linear response behavior seen in Sec. III B. Theoretically, the TDF spectra are described by the general formalism of the second-order optical processes.⁵⁶ With the above-mentioned assumption, it is shown straightforwardly that the TDF spectra with ultrafast and broad energy pulse excitations are well approximated by the time-dependent distribution function of the energy gap coordinate $P_{01}(\Delta V; t)$.

Figure 8 shows the resultant $P_{01}(\Delta V; t)$ obtained from the nonequilibrium trajectory calculations. The static distribution functions $P_I(\Delta V)$ from Fig. 2 are also included for comparison. The evolution of the average (or the centroid) of the distribution corresponds to the nonequilibrium response function $\Psi_{01}(t)$ in Fig. 4. On the other hand, because of the asymmetry of the actual distribution, the trace of the peak position is not precisely coincident with the response function. Interestingly, the direction of the asymmetry flips at certain intermediate time. Namely, the asymmetric deviation is toward the higher(lower) $-\Delta V$ at short(long) time. [See also the remarks around Eqs. (3.4)–(3.6).] Although beyond the scope of this paper, this behavior would be attributed to the (small) nonlinearity of the system, which might be elucidated by theories such as that in Ref. 50.

It is also seen that the width of the distribution function does not change very much in the nonequilibrium development. This is a consequence of the assumed broad energy photoexcitation. While relaxation and transient broadening of the excited state populations (and/or the ground state holes) created by narrow energy excitations are interesting issues, these would be suitably addressed for more slowly relaxing (e.g., glassy) systems.

E. Comparison with fixed-charge model

As described above, a quantum polarizable (Q-Pol) model of the dye probe is developed and examined. Here we aim to illuminate some characteristics of the model by comparing with a nonpolarizable model with fixed-charge parameters. For this purpose, we first determine the average atomic charges from the equilibrium simulations of the Q-Pol model (Table IV).⁴² The simulation procedure for this fixed-charge (Fix-Z) model is almost the same as that for Q-Pol described in Sec. II. The charges are automatically kept constant by simply nullifying the off-diagonal elements of the electronic energy matrix. The kinetic temperature in the equilibrium

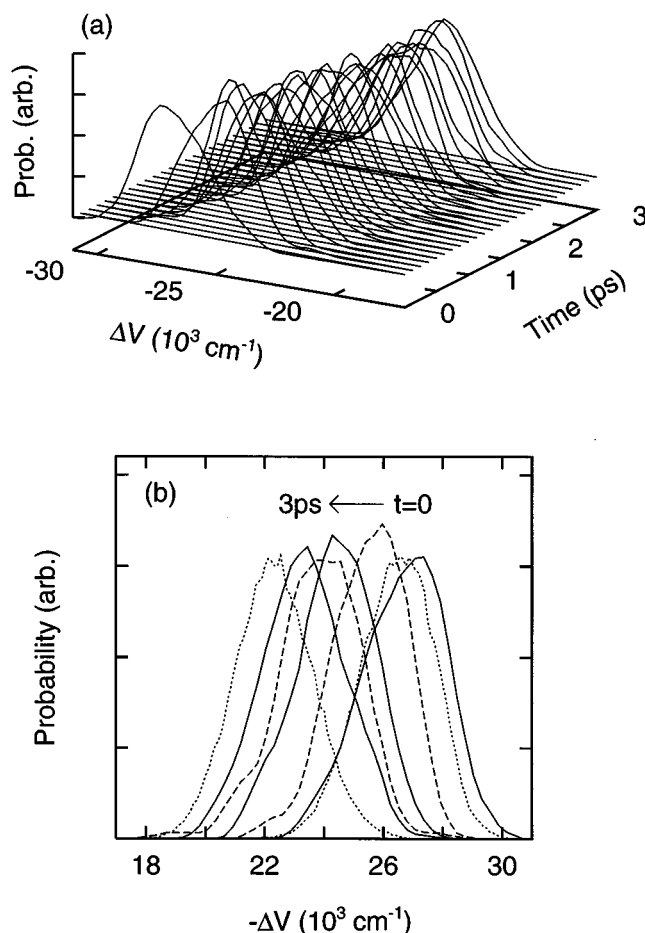


FIG. 8. The time-dependent distribution function of the energy gap coordinate $P_{01}(\Delta V; t)$, (a) with 0.125 ps interval and (b) at $t = 0, 0.1, 0.5, 1.5$, and 3.0 ps (solid and dashed curves). The dotted curves in (b) are the static equilibrium distributions from Fig. 2. Note the altered sign of the ΔV axis in (a), which is chosen for a convenient three-dimensional view.

simulation was 298 and 295 K for the S_0 and S_1 states, respectively, with rms fluctuations of ~ 7 K. The rms deviation of the total energy was typically 0.06 kcal/mol.

Figure 9 shows the TCFs and the response function for the Fix-Z model in comparison with those for Q-Pol as in Fig. 4. It appears that the solvation of the Q-Pol model is slower than that of Fix-Z. Indeed, a much more drastic slowdown of the solvation due to the solute electronic polarization has been observed in two recent simulation studies: Kumar and Maroncelli¹² examined a diatomic solute with a classical polarizability in acetonitrile and methanol solutions. Bursulaya *et al.*¹³ employed a quantum mechanical model of a polarizable point dipole in water. As both of them pointed out for their systems, the slowdown of solvation might be attributed to the reduction of the “solvent force constant,”⁵⁷

$$K_I = k_B T / \langle \delta \Delta V^2 \rangle_I = 1/2\lambda'_I. \quad (3.16)$$

Indeed, the apparent solvent force constant is notably smaller for Q-Pol, as seen from the λ'_I values in Table VI and from the distribution functions of Fig. 10(a) [see Eq. (3.6)]. However, the computed effective frequencies,

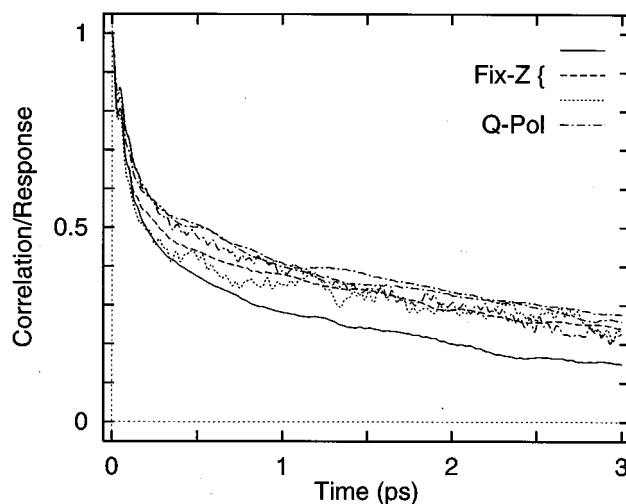


FIG. 9. The time correlation and the response functions $\Phi_0(t)$ (solid line), $\Phi_1(t)$ (dashed line), and $\Psi_{01}(t)$ (dotted line) for the fixed-charge (Fix-Z) model. The curves for the quantum-polarizable (Q-Pol) model (from Fig. 4) are drawn by dash-dotted lines.

$$\Omega_I = \sqrt{\langle \delta \Delta \dot{V}^2 \rangle_I / \langle \delta \Delta V^2 \rangle_I} \quad (= \sqrt{K_I/M_I}), \quad (3.17)$$

are not very different between the two models, as shown in Table VI. This reflects that the effective mass of the coordinate

$$M_I = k_B T / \langle \delta \Delta \dot{V}^2 \rangle_I \quad (3.18)$$

is also reduced for the Q-Pol model to almost cancel the reduction of the solvent force constant. Therefore, in this specific system, the solvent fluctuation dynamics *per se* is not quite dependent on the solute electronic polarization.

The distribution functions $P_I(\Delta V)$ and the first-order spectra are compared in Figs. 10(a) and 10(b). It is seen that the Fix-Z model gives a much smaller peak shift and widths of $P_I(\Delta V)$ than Q-Pol, which reflects the smaller reorganization energies λ and λ'_I , respectively. The computed λ and λ'_I are included in Table VI. It is also seen that the discrepancy between λ and λ'_I is smaller for Fix-Z than that for Q-Pol. In other words, the solute electronic polarization causes larger amplitude of the ΔV fluctuation. (It is noted that ΔV for Q-Pol includes the variation of the solute electronic energies besides the solute-solvent interactions.) The FWHM and the Stokes shift of the spectra for Fix-Z are listed in Table VIII, both of which are notably smaller than those for Q-Pol. As seen in Fig. 10, the comparison between the two models for $P_I(\Delta V)$ is nearly parallel to that for the spectra.

IV. CONCLUDING REMARKS

In this work we have studied the solvation dynamics of C120 in methanol. It is shown that a proper modeling of the solvent-induced electronic polarization of the solute probe notably affects the solvation dynamics and especially the

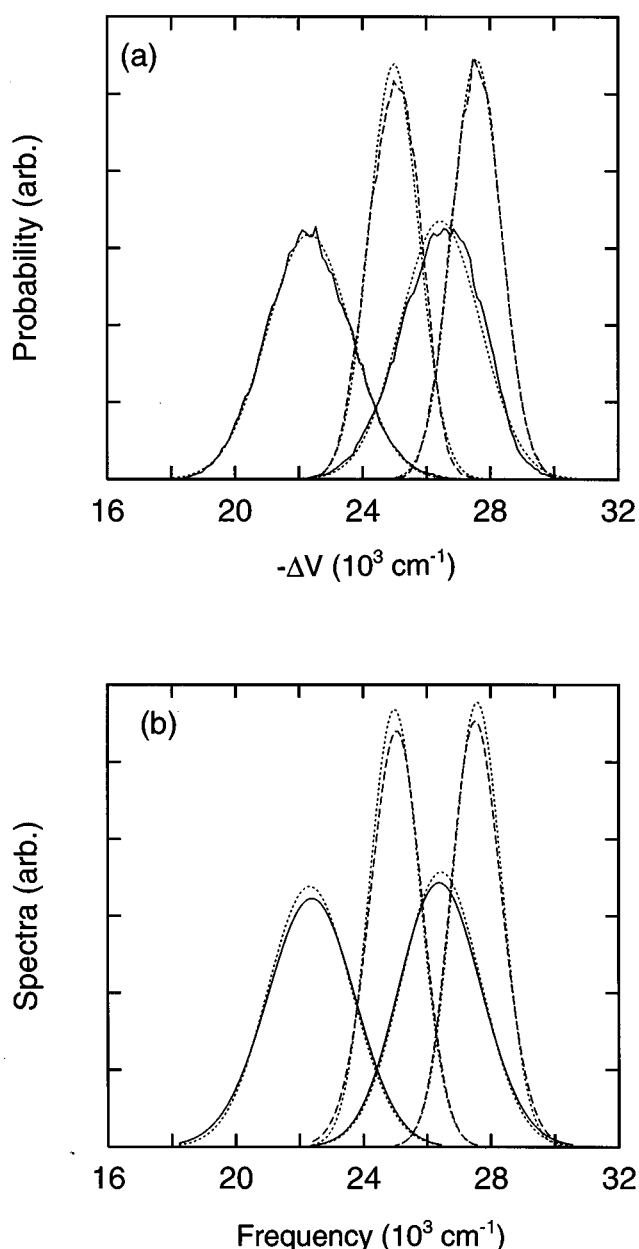


FIG. 10. Comparison between the quantum-polarizable (Q-Pol, solid line) and the fixed-charge (Fix-Z dashed line) models for the probability distribution functions $P_I(\Delta V)$ (a) and for the absorption/fluorescence spectra (b). The plots for Q-Pol are from Figs. 2 and 7. The dotted curves are the Gaussians of Eq. (3.4) (a) and of the classical ($\beta\hbar \rightarrow 0$) limit (b).

spectral linewidths and the Stokes shift. We inspect many of the perspectives exploited here would also carry over for other 7-amino coumarin series.

Because the solute C120 is treated as a rigid body in the present modeling, the computed spectral widths represent only the solvent-induced (“inhomogeneous”²⁵) broadening. Extensive modelings incorporating the solute intramolecular vibrations, to account for the vibronic transitions and the vibrational dephasing mechanisms, are needed to further compare with experiments. (On the other hand, experimental analyses would be aiming at extracting the purely solvent-

induced component from the real spectra.⁵⁸) Nonetheless, we speculate that the reorganization energy for the Fix-Z model is too small to reproduce the experimental spectra, in particular the large Stokes shift of $\sim 5000 \text{ cm}^{-1}$, even if the vibronic transitions were taken into account.

When modeling the solute intramolecular vibrations, it would be consistent to employ flexible models of the solvent as well to effect the solute–solvent vibrational energy transfers. In that case, notable quantum effects of the stretching and bending modes of the methanol hydroxyl part would also manifest, which contribute to broaden the spectra asymmetrically by extending the outer tails of the absorption/fluorescence spectra. This aspect is theoretically isomorphic with the marked quantum tunneling effects of the solvent high-frequency modes in the inverted regimes of electron transfers, which give rise to asymmetric (nonparabolic) energy gap law.⁵³ (See also the discussion pertaining to Fig. 7.)

Another possibly important issue that is not addressed here would be the role of the large amplitude intramolecular wagging and torsional motions of the amino group of C120. (In this respect, the present system might rather be viewed as a model of the rigid 7-amino coumarins.) For real C120 (and other flexible 7-amino coumarins), this may affect the electronic structure of the solute, adding, in particular, a possibility of the twisted intramolecular charge transfer (TICT) state formation.^{16,22,59,60} To our knowledge, the double fluorescence characteristic of the TICT systems has not been observed for 7-amino coumarins. However, decay paths via nonradiative transitions might affect the spectral line shapes.

Additionally, there is a specific chemical issue for the 7-amino coumarins regarding the competing basicities of the amino and carbonyl groups¹⁷ that depend on the electronic states and on the hydrogen bonding with protic solvents. Microscopic details of these aspects and their consequences on the optical responses are yet unclear. More accurate electronic wave functions and interaction potential functions, capable of adequately describing the charge-transfer type interactions, would be required to clarify these issues.

ACKNOWLEDGMENTS

This work was initiated with support by a Special Postdoctoral Researchers Program at RIKEN and was completed with a grant from the University of Tsukuba Research Projects. Numerical calculations were carried out at the RIKEN Supercomputer Center and at the Science Information Processing Center of the University of Tsukuba. The author is grateful to Dr. A. Kira and the members of Chemical Dynamics Lab at RIKEN for their encouragement. He also benefited from discussions at The 56th Okazaki Conference (September 1996) at which part of this work has been presented.

APPENDIX A

For the current purpose of devising adiabatic simulations, a compact description of the diabatic electronic bases is useful. Generally, the electronic polarization of molecules is described by mixing (primarily single-electron) excitation

configuration state functions (CSFs) to the reference HF wave function. This is precise when all possible CSFs were considered. We examine here how efficiently the polarized $|\phi_{\text{pol}}^0\rangle$ (from the SCRF calculations) can be approximated by augmenting single-excitation CSFs within the orbital space for $|\phi_{\text{np}}^0\rangle$, i.e.,

$$|\phi_{\text{pol}}^0\rangle = C_0|\phi_{\text{np}}^0\rangle + \sum_{(a \rightarrow r)} C_a^r |\phi_{\text{np}}^0(a \rightarrow r)\rangle + \cdots, \quad (\text{A1})$$

where $|\phi_{\text{np}}^0(a \rightarrow r)\rangle$ denotes the (spin-symmetrized) CSF with the single excitation from the occupied a to the vacant r orbitals. The coefficients are given by

$$C_0 = \langle \phi_{\text{np}}^0 | \phi_{\text{pol}}^0 \rangle, \quad (\text{A2})$$

$$C_a^r = \langle \phi_{\text{np}}^0(a \rightarrow r) | \phi_{\text{pol}}^0 \rangle. \quad (\text{A3})$$

Among the coefficients computed within the 12 π -like active orbitals of C120 (the occupied 5 π and 2 lone pairs and the unoccupied 5 π^*), C_0 and the HOMO (highest occupied MO) to LUMO (lowest unoccupied MO) excitation configuration are found to account for 92% and 3.8% of $|\phi_{\text{pol}}^0\rangle$, respectively. However, the remaining contributions are no larger than 0.35% per CSF, showing quite slow convergence for the rest of the polarization.

APPENDIX B

The spectral density function $J(\omega)$ for two-state harmonic systems broadly employed in the literature⁶¹ would be specified by the following sum relation:

$$\lambda = \frac{4}{\pi} \int_0^\infty \frac{J(\omega)}{\omega} d\omega, \quad (\text{B1})$$

or be expressed as

$$J(\omega) = \frac{\pi}{2} \sum_\alpha \frac{c_\alpha^2}{\omega_\alpha} \delta(\omega - \omega_\alpha), \quad (\text{B2})$$

where c_α denotes the coupling constant for the α th bath mode of frequency ω_α . For exactly harmonic cases, the presently employed $G^q(\omega)$ and $G^{\text{cl}}(\omega)$ are related to $J(\omega)$ by

$$J(\omega) = \frac{\beta\omega}{8} G^{\text{cl}}(\omega) = \frac{e^{\beta\hbar\omega} - 1}{8\hbar} G^q(\omega). \quad (\text{B3})$$

¹ P. G. Wolynes, *Annu. Rev. Phys. Chem.* **31**, 345 (1984); J. T. Hynes, in *The Theory of Chemical Reaction Dynamics*, edited by M. Baer (Chemical Rubber, Boca Raton, FL, 1985), Vol. 4.

² E. M. Kosower and D. Huppert, *Annu. Rev. Phys. Chem.* **37**, 127 (1986); P. F. Barbara and W. Jarzeba, *Acc. Chem. Res.* **21**, 195 (1988); P. J. Rossky and J. D. Simon, *Nature (London)* **370**, 263 (1994).

³ (a) *Ultrafast Reaction Dynamics and Solvent Effects: Theoretical and Experimental Aspects*, edited by Y. Gauduel and P. J. Rossky (AIP, New York, 1994); (b) G. R. Fleming and M. Cho, *Annu. Rev. Phys. Chem.* **47**, 109 (1996).

⁴ B. M. Ladanyi and M. S. Skaf, *Annu. Rev. Phys. Chem.* **44**, 335 (1993).

⁵ M. Rao and B. J. Berne, *J. Phys. Chem.* **85**, 1498 (1981); O. A. Karim, A. D. J. Haymet, M. J. Banet, and J. D. Simon, *ibid.* **92**, 3391 (1988); M. Maroncelli and G. R. Fleming, *J. Chem. Phys.* **89**, 5044 (1988).

⁶ T. Fonseca and B. M. Ladanyi, *J. Phys. Chem.* **95**, 2116 (1991); *J. Mol. Liq.* **60**, 1 (1994).

⁷ M. Maroncelli, *J. Chem. Phys.* **94**, 2034 (1991); E. A. Carter and J. T. Hynes, *ibid.* **94**, 5961 (1991).

⁸ R. M. Levy, D. B. Kitchen, J. T. Blair, and K. Krogh-Jespersen, *J. Phys. Chem.* **94**, 4470 (1990); M. Belhadj, D. B. Kitchen, K. Krogh-Jespersen, and R. M. Levy, *ibid.* **95**, 1082 (1991).

⁹ K. Ando and S. Kato, *J. Chem. Phys.* **95**, 5966 (1991).

¹⁰ (a) S. J. Rosenthal, R. Jimenez, G. R. Fleming, P. V. Kumar, and M. Maroncelli, *J. Mol. Liq.* **60**, 25 (1994); (b) R. Jimenez, G. R. Fleming, P. V. Kumar, and M. Maroncelli, *Nature (London)* **369**, 471 (1994).

¹¹ R. Brown, *J. Chem. Phys.* **102**, 9059 (1995).

¹² P. V. Kumar and M. Maroncelli, *J. Chem. Phys.* **103**, 3038 (1995).

¹³ B. D. Bursulaya, D. A. Zichi, and H. J. Kim, *J. Phys. Chem.* **99**, 10069 (1995); **100**, 1392 (1996).

¹⁴ I. Ohmine, *J. Chem. Phys.* **85**, 3342 (1986); P. Ilich, C. Haydock, and F. G. Prendergast, *Chem. Phys. Lett.* **158**, 129 (1989); P. L. Muiño and P. R. Callis, *J. Chem. Phys.* **100**, 4093 (1994).

¹⁵ J. T. Blair, K. Krogh-Jespersen, and R. M. Levy, *J. Am. Chem. Soc.* **111**, 6948 (1989); V. Luzhkov and A. Warshel, *ibid.* **113**, 4491 (1991); S. Ten-no, F. Hirata, and S. Kato, *J. Chem. Phys.* **100**, 7443 (1994); K. Ando and J. T. Hynes, *J. Mol. Liq.* **64**, 25 (1995); *J. Phys. Chem.* (in press).

¹⁶ S. Kato and Y. Amatatsu, *J. Chem. Phys.* **92**, 7241 (1990); S. Hayashi, K. Ando, and S. Kato, *J. Phys. Chem.* **99**, 955 (1995).

¹⁷ K. H. Drexhage, in *Dye Lasers*, edited by F. P. Schäfer (Springer, Berlin, 1973).

¹⁸ N. P. Ernsting, M. Asimov, and F. P. Schäfer, *Chem. Phys. Lett.* **91**, 231 (1982).

¹⁹ M. A. Kahlou, T. J. Kang, and P. F. Barbara, *J. Chem. Phys.* **88**, 2372 (1988); H. Shirota, H. Pal, K. Tominaga, and K. Yoshihara, *J. Phys. Chem.* **100**, 14575 (1996); M. L. Hornig, J. A. Gardecki, A. Papazyan, and M. Maroncelli, *ibid.* **99**, 17311 (1995), and references therein.

²⁰ M. Maroncelli and G. R. Fleming, *J. Chem. Phys.* **86**, 6221 (1987).

²¹ G. A. Reynolds and K. H. Drexhage, *Opt. Commun.* **13**, 222 (1975); R. F. Kubin and A. N. Fletcher, *Chem. Phys. Lett.* **99**, 49 (1983).

²² G. Jones II, W. R. Jackson, C. Choi, and W. R. Bergmark, *J. Phys. Chem.* **89**, 294 (1985).

²³ Recently, a possible role of multielectronic (involving S_2 and triplet) states in the polar solvation of coumarin 153 was suggested; Y. Jiang, P. K. McCarthy, and G. J. Blanchard, *Chem. Phys.* **183**, 249 (1994).

²⁴ There could be a specific counteracting effect for those 7-amino coumarins having one or two amino hydrogen atoms. For example, C120 absorbs at a shorter wavelength in HFIP (hexafluoroisopropanol) than in methanol, which is suggested to be due to the specificity of the $-\text{NH}_2$ group (see Ref. 17).

²⁵ Throughout this paper, the term “inhomogeneous” may read instead as “solvent-induced.” In disordered systems at low temperatures, the former is rather specifically associated with the nonequilibrium distribution of the transition energy, which is indeed closely connected to the latter at high temperatures.

²⁶ We used the program MOPAC Version 6 for the MNDO calculations; J. J. P. Stewart, MOPAC6.0, QCPE 455. For the semiempirical MNDO approximation; M. J. S. Dewar and W. Thiel, *J. Am. Chem. Soc.* **99**, 4899 (1977).

²⁷ An optimization without this constraint is also carried out. The deviations of the dihedral angles from the planar geometry are smaller than 0.5° except that the $\text{NC}_7\text{C}_6\text{C}_5$ torsion resulted in 174.3° .

²⁸ We used the programs HONDO7 and GAMESS for the standard *ab initio* self-consistent field, SCRF, and S-CI calculations. HONDO7; M. Dupuis, J. D. Watts, H. O. Villar, and G. J. B. Hurst, HONDO Version 7.0, QCPE 544 (1987); Comput. Phys. Comm. **52**, 415 (1989). GAMESS; M. W. Schmidt *et al.*, *J. Comput. Chem.* **14**, 1347 (1993). The corresponding orbital transformations and the subsequent calculations of the energy and dipole matrices and the exchange potentials are carried out with codes written to interface to the HONDO7 package.

²⁹ For the open-shell singlet ROHF calculation; E. R. Davidson, *Chem. Phys. Lett.* **21**, 565 (1973); F. W. Bobrowicz and W. A. Goddard, in *Methods of Electronic Structure Theory, Modern Theoretical Chemistry Vol. 3*, edited by H. F. Schaefer (Plenum, New York, 1977).

³⁰ For example, M. Szafran, M. M. Karelson, A. R. Katritzky, J. Koput, and M. C. Zerner, *J. Comput. Chem.* **14**, 371 (1993).

³¹ (a) H. F. King, R. E. Stanton, H. Kim, R. E. Wyatt, and R. G. Parr, *J. Chem. Phys.* **47**, 1936 (1967). (b) For example, M. Dupuis, A. Farazdel, S. P. Karna, and S. A. Maluendes, in *MOTECC: Modern Techniques in*

- Computational Chemistry*, edited by E. Clementi (ESCOM, Leiden, 1990).
- ³²I. D. Petsalakis, G. Theodorakopoulos, C. A. Nicolaides, R. J. Buenker, and S. D. Peyerimhoff, *J. Chem. Phys.* **81**, 3161 (1984); P. C. Hiberty, J. P. Flament, and E. Noizet, *Chem. Phys. Lett.* **189**, 259 (1992); N. Tomita, S. Ten-no, and Y. Tanimura, *ibid.* **263**, 687 (1996).
- ³³H. Tatewaki and S. Huzinaga, *J. Comput. Chem.* **1**, 205 (1980).
- ³⁴In the S-CI calculation, the lowest 13 orbitals representing the 1s core orbitals of C, N, and O atoms are kept doubly occupied (frozen). The number of configuration state functions generated by single excitations from the remaining 33 occupied to 89 vacant orbitals is 2938. The dominance of the $n\pi^*$ -type configurations is first seen for the S_3 state.
- ³⁵We choose the experimental static dielectric constant (ϵ_0) of water although the present study is for the methanol solution of the smaller $\epsilon_0 = 33.7$. The idea is to obtain strongly polarized diabatic basis to be used in the adiabatic simulation. However, the SCRF results are expected to be rather insensitive to these numbers because they enter into the factor $2(\epsilon_0 - 1)/(2\epsilon_0 + 1)$.
- ³⁶We have also carried out the SCRF calculations with 4.0 and 3.0 Å cavity radii. The calculation with a 3.0 Å radius did not converge for both the S_0 and S_1 states. As stated in the text, we employ the results obtained with 3.5 Å (i.e., more polarized ones) rather than those with a 4.0 Å radius.
- ³⁷As expected generally, the ROHF approximation itself does not give quantitative dipole moment of excited states. (Compare the results in Table II.) It would be intriguing to see, however, that by mixing the nonorthogonal Slater determinants the adiabatic simulation results show the expected increase of the dipole moment of C120 upon photoexcitation. (See also Ref. 32.)
- ³⁸A constant correction is introduced into the diagonal energy elements so that the gas-phase S_0 – S_1 excitation energy reproduces the estimated 0–0 excitation energy of C120. This correction is mostly relevant to the absolute energy locations of the absorption/fluorescence spectra, and is not quite essential for the primary results (the time correlation functions, the spectral line shapes, and the Stokes shifts) of the present work. The 0–0 excitation energy ν_{00} of C120 is estimated from a series of available experimental data (Refs. 18 and 20) for C153, C102, and C151. This includes the peak frequency of the absorption band in methanol and trifluoroethanol (TFE) solutions $\bar{\nu}_{(\text{MeOH})}$ and $\bar{\nu}_{(\text{TFE})}$. First we estimate ν_{00} of C102 from ν_{00} , $\bar{\nu}_{(\text{MeOH})}$, and $\bar{\nu}_{(\text{TFE})}$ of C153, by assuming that the ratio $(\nu_{00} - \bar{\nu}_{(\text{MeOH})})/(\bar{\nu}_{(\text{MeOH})} - \bar{\nu}_{(\text{TFE})})$ is the same between C102 and C153. This estimates $\nu_{00}(\text{C102}) = 27.27 \times 10^3 \text{ cm}^{-1}$. Then, ν_{00} of C120 is evaluated by assuming $\nu_{00}(\text{C153}) - \nu_{00}(\text{C151}) = \nu_{00}(\text{C120}) - \nu_{00}(\text{C102})$, which finally gives $\nu_{00}(\text{C120}) = 30.13 \times 10^3 \text{ cm}^{-1}$. Because we treat the solute C120 as a rigid body, the computed excitation energy does not precisely correspond to the 0–0 excitation energy. Nonetheless, the rough estimate of the correction employed here would be enough for the present purpose.
- ³⁹(a) For example, U. C. Singh and P. A. Kollman, *J. Comput. Chem.* **5**, 129 (1984); (b) M. L. Connolly, *Science* **221**, 709 (1983).
- ⁴⁰H. J. Kim and J. T. Hynes, *J. Chem. Phys.* **96**, 5088 (1992).
- ⁴¹(a) W. L. Jorgensen and J. Tirado-Rives, *J. Am. Chem. Soc.* **110**, 1657 (1988); (b) W. L. Jorgensen, *ibid.* **103**, 335 (1981); (c) *J. Phys. Chem.* **90**, 1276 (1986).
- ⁴²Although the atomic charges over $\pm e$ in Table IV may appear too big, these cause essentially no problem in the present calculations because the physically relevant quantity is the net interaction potential summed over the solute atomic sites in Eq. (2.2) which is most adequately modeled by the ESP-derived charges. If one is to discuss details of each atomic charge, alternative methods such as the Natural Population Analysis [A. E. Reed, R. B. Weinstock, and F. Weinhold, *J. Chem. Phys.* **83**, 735 (1985)] would be suitable. For semiempirical atomic charges of coumarin 1, see; P. K. McCarthy and G. J. Blanchard, *J. Phys. Chem.* **97**, 12205 (1993).
- ⁴³(a) M. P. Allen and D. J. Tildesley, *Computer Simulation of Liquids* (Clarendon, Oxford, 1987); (b) D. J. Adams, *Chem. Phys. Lett.* **62**, 329 (1979); (c) C. W. Gear, *Numerical Initial Value Problems in Ordinary Differential Equations* (Prentice-Hall, Englewood Cliffs, 1971); (d) for example, W. L. Press, B. P. Flannery, S. A. Teukolsky, and W. T. Vetterling, *Numerical Recipes: The Art of Scientific Computing* (Cambridge University Press, New York, 1989).
- ⁴⁴We take the following two-step procedure for the solute electronic part: First, the 2×2 Hamiltonian matrices on $|\phi_{\text{np}}\rangle$ and $|\phi_{\text{pol}}\rangle$ bases are solved for each of the S_0 and S_1 states. Then the 2×2 Hamiltonian on the S_0 and S_1 wave functions thus obtained is constructed to be diagonalized. The purpose of the first step is to characterize the solute polarization in terms of the fluctuation between the two bases. The second step could have been omitted for simplification if the transition properties such as the transition dipoles were not of major interest. (As an alternative option, our simulation code can directly handle the 4×4 Hamiltonian matrix constructed from the four diabatic bases. General an $N \times N$ description is also possible—besides the computational limitation—which will be presented elsewhere.)
- ⁴⁵Cooling and equilibration runs were carried out prior to the production runs reported in the text. In the cooling run, the translational and angular velocities of the molecules are scaled to 298 K at every 3000 steps (=1.5 ps), which is repeated at least 20 times. Then, the equilibration run is performed for 30 ps by using the constant temperature method by Berendsen *et al.* to keep the kinetic temperature around 298 K. The relaxation time parameter of the method was set to be 0.4 ps, see H. J. C. Berendsen, J. P. M. Postma, W. F. van Gunsteren, A. Di Nola, and J. R. Haak, *J. Chem. Phys.* **81**, 3684 (1984).
- ⁴⁶M. Tachiya, *J. Phys. Chem.* **97**, 5911 (1993); M. Tachiya and M. Hilczler, in Ref. 3(a).
- ⁴⁷Although this behavior is seen in both the equilibrium and nonequilibrium distributions, the deviations from the Gaussian are very small. Therefore, it would be intriguing to pursue this issue for (some modelistic) systems with increased nonlinearity.
- ⁴⁸Equation (3.5) is appreciated in the electron transfer context: M. Tachiya, *J. Phys. Chem.* **93**, 7050 (1989); A. Yoshimori, T. Kakitani, Y. Enomoto, and N. Mataga, *ibid.* **93**, 8316 (1989).
- ⁴⁹The previous works which show a larger nonlinearity of methanol solvation deal with greater perturbations associated with ionizations, dipole creations, or dipole flips of spherical or diatomic solute. On the other hand, as in Refs. 9, 11, and 12, the linear response behavior has been observed for polyatomic solutes in which the changes in the charges are distributed.
- ⁵⁰For a theory of nonlinear effects in polar solvation dynamics, see A. Yoshimori, *Chem. Phys. Lett.* **184**, 76 (1991); *J. Mol. Liq.* **65/66**, 297 (1995).
- ⁵¹M. Lax, *J. Chem. Phys.* **20**, 1752 (1952); R. Kubo and Y. Toyozawa, *Prog. Theor. Phys.* **13**, 160 (1955).
- ⁵²For example, M_{ab} may be given by the semiclassical approximation $M_{ab} = \mathbf{d}_i \cdot \mathbf{E}$ where \mathbf{E} denotes the classical electric field vector of the incident light, and $M_{\text{fl}} \propto \mathbf{d}_i \cdot \mathbf{e}$ where \mathbf{e} represents one of the polarization vectors of the emitting photon.
- ⁵³K. Ando, *J. Chem. Phys.* **106**, 116 (1997).
- ⁵⁴The cosine transform of the TCF is computed from the power spectrum of the ΔV trajectory (the Wiener–Khinchin theorem), by using the FFT (fast Fourier transform) method. The Bartlett window was applied to reduce the finite truncation bias [Ref. 43(d)]. The 9×10^5 steps (=450 ps) data were divided into and averaged over 109 parts with the length of 2^{13} steps. This length gives the frequency resolution of 8.1 cm^{-1} .
- ⁵⁵It would be of interest to compare with the water solvent. The oscillation in the TCF coming from the libration is seen more prominently and the libration peak band of the spectral density is relatively more intense for aqueous solutions. See Ref. 53, for example.
- ⁵⁶See, for example, R. Kubo, M. Toda, and N. Hashitsume, *Statistical Physics II: Nonequilibrium Statistical Mechanics* (Springer, New York, 1985); S. Kinoshita and Y. Kanematsu, in *Advances in Multi-photon Processes and Spectroscopy*, edited by S. H. Lin, A. A. Villaes, and Y. Fujimura (World Scientific, Singapore, 1995), Vol. 9.
- ⁵⁷The variances $\langle \delta \Delta V^2 \rangle_t$ and $\langle \delta \Delta \dot{V}^2 \rangle_t$ in the expressions of λ'_i , M_I , K_I , and Ω_I are classical quantities directly evaluated by the MD simulations.
- ⁵⁸See, for example, J. Yu and M. Berg, *J. Chem. Phys.* **96**, 8741 (1992).
- ⁵⁹For a review on TICT, see, for example, W. Rettig, *Angew. Chem., Int. Ed. Engl.* **25**, 971 (1986).
- ⁶⁰The $-\text{NH}_2$ group of C120 has less possibility of the TICT state formation than the other amino groups with the electron-donating alkyl groups— NRR' ($\text{R}, \text{R}' = \text{CH}_3, \text{C}_2\text{H}_5$, etc.).
- ⁶¹See, for example, A. J. Leggett, S. Chakravarty, A. Dorsey, M. P. A. Fisher, A. Garg, and W. Zwerger, *Rev. Mod. Phys.* **59**, 1 (1987), and references therein.